

Nonlinear Inverse Design of Mechanical Multi-Material Metamaterials Enabled by Video Denoising Diffusion and Structure Identifier

Jaewan Park^{1,2}, Shashank Kushwaha¹, Junyan He¹, Seid Koric^{1,2*}, Qibang Liu^{2,3}, Iwona Jasiuk¹, Diab Abueidda^{2,4*}

¹ *Department of Mechanical Science and Engineering, University of Illinois at Urbana-Champaign, Urbana, IL, USA*

² *National Center for Supercomputing Applications, University of Illinois at Urbana-Champaign, Urbana, IL, USA*

³ *Department of Industrial and Manufacturing Systems Engineering, Kansas State University, Manhattan, KS, USA*

⁴ *Civil and Urban Engineering Department, New York University Abu Dhabi, United Arab Emirates*

Abstract

Metamaterials, synthetic materials with customized properties, have emerged as a promising field due to advancements in additive manufacturing. These materials derive unique mechanical properties from their internal lattice structures, which are often composed of multiple materials that repeat geometric patterns. While traditional inverse design approaches have shown potential, they struggle to map nonlinear material behavior to multiple possible structural configurations. This paper presents a novel framework leveraging video diffusion models, a type of generative artificial Intelligence (AI), for inverse multi-material design based on nonlinear stress-strain responses. Our approach consists of two key components: (1) a fields generator using a video diffusion model to create solution fields based on target nonlinear stress-strain responses, and (2) a structure identifier employing two UNet models to determine the corresponding multi-material 2D design. By incorporating multiple materials, plasticity, and large deformation, our innovative design method allows for enhanced control over the highly nonlinear mechanical behavior of metamaterials commonly seen in real-world applications. It offers a promising solution for generating next-generation metamaterials with finely tuned mechanical characteristics.

Keywords: Generative AI, Diffusion model, Inverse design, Multi-material design, Plastic deformation

1. Introduction

The concept of producing artificial materials with customized characteristics has become increasingly popular in many engineering fields since additive manufacturing allows for the fabrication of architected materials, also known as metamaterials, at various scales and sizes [1]. Unique mechanical properties of metamaterials, such as how they bend, stretch, compress, or respond to forces, come from the material's internal structure, often made up of repeating geometric patterns

*Corresponding author

Email addresses: koric@illinois.edu (Seid Koric^{1,2}), abueidd2@illinois.edu (Diab Abueidda^{2,4})

of multiple conventional materials. Opposite to the restricted range of natural bulk materials, engineers and designers now have the opportunity to explore the significantly broadened design and property possibilities of metamaterials. These materials have been specifically developed to accomplish mechanical properties and behaviors that were previously unattainable, such as in impact energy absorption in automotive and aerospace industries [2], soft robotics and actuators that can undergo large and irreversible deformations in response to external loadings [3], and bio-inspired materials for that mimic the nonlinear mechanical properties and behavior of biological tissues for use in tissue engineering or medical implants and prosthetic [4]. Recent advancements in multi-material additive manufacturing have further expanded the possibilities for designing and fabricating complex lattice structures [1]. Such capability allows for more precise control over the mechanical properties and behavior of metamaterials, opening up new avenues for innovative designs and applications.

Historically, the forward approaches [5–8] were used to systematically modify the design parameters of complex and architected materials until the measured or simulated properties meet specifically defined design requirements. These methods typically need significant prior knowledge of experienced designers, and they are burdened by computationally demanding simulations of iterative experiments, especially for materials exhibiting intricate, nonlinear characteristics. On the other hand, topology optimization (TO) methods, including gradient-based algorithms and genetic algorithms [9–12], and traditional non-generative machine learning-based design approaches [13–18], as reviewed in [19], have shown potential for achieving desired property values. However, these methods face several challenges when dealing with complex, nonlinear material behaviors. While TO can be extended to various types of nonlinearities [20], such extensions are mathematically rigorous, and their implementation is prone to errors. Additionally, TO methods often struggle with getting trapped in local minima, particularly for highly nonlinear problems. Furthermore, the non-unique mapping between mechanical responses and structural designs, inherent in many meta-material design problems, poses a significant challenge for these approaches.

Generative artificial intelligence models represent a category of artificial intelligence systems engineered to produce novel data that emulates patterns found in existing data. Generative models differ from traditional AI models, primarily focused on recognizing patterns or making predictions based on input data. Instead, generative models seek to produce novel outputs that mimic the training data’s characteristics, making them attractive for nonlinear inverse design [21, 22]. Mao et al. [23] used a generative adversarial network (GAN) to design architected materials while Zheng et al. [24] proposed an inverse design method for auxetic metamaterials using a conditional generative adversarial network cGAN. Ma et al. [25] and Wang et al. [26] used a conditional variational autoencoder (VAE) to generate a metamaterial structure with specific mechanical properties. Recently, Ha et al. [27] implemented a generative machine learning (ML) pipeline composed of inverse prediction and forward validation modules.

Among generative AI models, diffusion models [28] have shown exceptional achievements in several domains of AI, notably in generating images and videos. Diffusion models are ML methods that gradually transform random noise into meaningful data, like images or videos. Starting with a clear image or a video, the model first adds random noise until it becomes unrecognizable and pure noise. Once the model learns how the noise is added, it reverses the process by gradually denoising it step by step, transforming the noise back into something recognizable and comparing it with its original image or video target. By repeating this training process with many data samples, the model eventually learns to generate new images or videos from random noise data it has never seen

before. The newly generated images or videos look realistic and match the patterns learned from the original data. To create images or videos on specific conditional class, Dhariwal and Nichol [29] proposed a classifier guidance method that trains a classifier on noise images and uses the gradient of the classifier to guide the sampling toward the target class. Later, Ho and Salimans [30] proposed a classifier-free guidance method that uses the scores from a conditional diffusion and an unconditional diffusion model, allowing the model to learn to generate fields both conditionally and unconditionally. Such diffusion models have been widely used in current popular AI applications, such as DALL-E-2 [31], DALL-E-3 [32], and Sora [33, 34] developed by OpenAI, Imagen Video [35, 36] by Google Research Brain Team, Stable Diffusion [37–39] by Stability AI, Midjourney by Minjourney Inc, and NAI diffusion by NovelAI. Beyond image or video synthesis in these tools, application of conditional diffusion models has expanded recently to encompass disciplines such as design for material science, including molecular design [40–42], single metamaterial architecture design [43–46], superconductors design [47, 48] and many others, where they reveal promise for addressing highly challenging and often unsolvable inverse design problems.

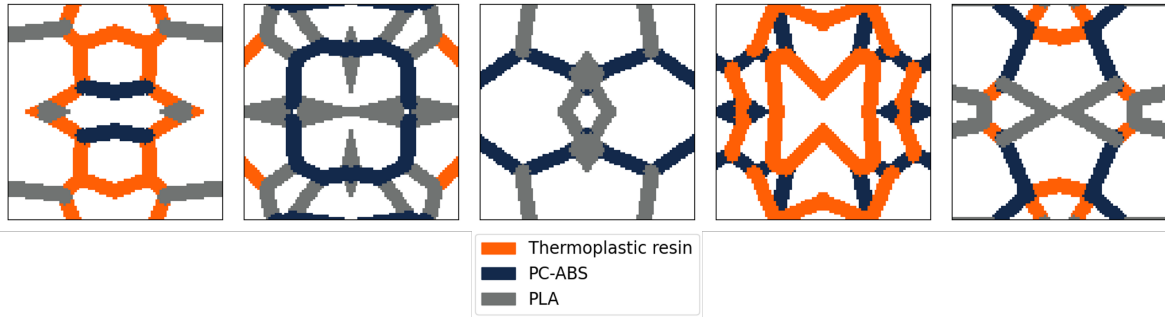
This paper presents a novel framework that leverages a video diffusion model that performs inverse multi-material design. Our approach is specifically tailored to generate designs with multiple materials that satisfy a given nonlinear stress-strain response. The application of diffusion models to video data incorporates temporal dynamics, enabling the model to accurately represent the dynamic changes that occur over time, similar to the evolution of deformation paths in nonlinear mechanical quasi-static behavior. The capacity to represent both spatial and temporal relationships renders video diffusion models suitable for challenges involving the evolution of system changes over time, such as in nonlinear deformation under stress. Bastek and Kochmann [43] used this concept, inspired by [35, 36], to design periodic stochastic cellular structures under compression loading in the large-strain hyper-elastic regime, including buckling and contact. However, their landmark work involved a single material, which enabled a simple mapping methodology to predict material distribution from the predicted solution fields. To the best of our knowledge, no previous research work has devised a general diffusion model framework to predict metamaterial designs with multiple materials. Such problem is very important since designers can further fine-tune the metamaterial’s overall behavior by using different materials, each with unique mechanical, thermal, or electrical properties. For example, one material might provide stiffness while another offers compliance, allowing for a balance between strength and deformability. In addition, we included plastic deformation, an irreversible behavior common to many materials under large deformation that exceeds yielding. Conversely, this also introduced additional challenges to our diffusion model in learning deformation path-dependent highly nonlinear material behavior.

2. Methods

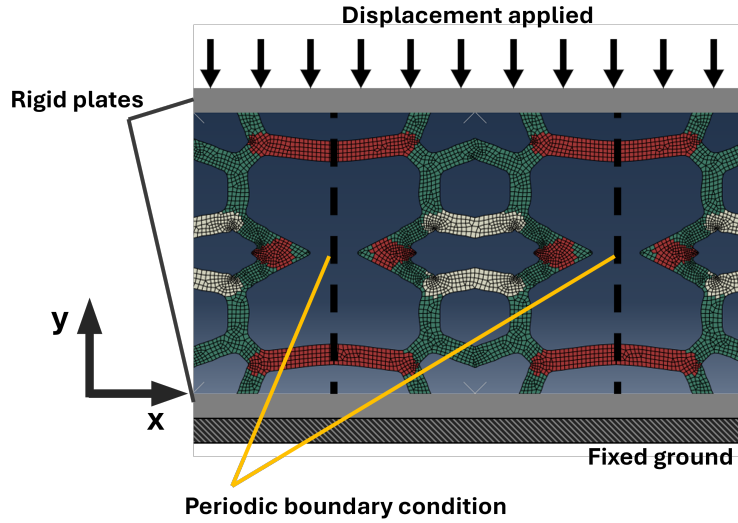
2.1. Training data generation

We generate truss-like multi-material metamaterials based on random Voronoi tessellations [49]. The initial step involves generating random points in a 2D space and using these points to create finite Voronoi polygons through the Voronoi function in the Python library *scipy.spatial*. The method constructed Voronoi diagrams, which are then used to extract polygon edges representing the boundaries between regions. Each of these edges is randomly assigned one of three material types, forming the basis of the material distribution. Following this, the polygon edges are

thickened. Therefore, each edge becomes a truss-like feature in the design. For simplicity of representing the designs and using the design information as inputs to the diffusion model, the thickened design is then projected to a structured grid to be stored as a 2D array of shape 48×48 , where each pixel stores the material ID (0 for void, 1-3 for the three different materials). To construct a symmetric and periodic design, each instantiation is considered as one-quarter of the full design, and the full design is recovered from sequential mirroring along two in-plane directions. The use of random Voronoi tessellations leads to metamaterials with varying relative density, further leading to design space with a wide range of stress-strain responses. Furthermore, this pixel-based representation makes it ideal for use in finite element simulations. Thus, this method provides a flexible approach for generating non-regular, multi-material distributions with varying degrees of complexity, applicable to broad engineering applications. Selected example designs are shown in Fig. 1a.



(a) Examples of multi-material designs created using Voronoi polygons



(b) Finite element setting to obtain field values and stress-strain curve of the whole structure.

Figure 1: Designs examples and FEA setting of the problem

Once the designs are generated, nonlinear implicit dynamic analysis is performed using general purpose finite element analysis (FEA) code [50], solving combined nonlinearities originating from large deformation and plastic material response. As shown in Fig. 1b, designs are placed

between two rigid plates, and a quasi-static compression load is applied by moving the top plate and keeping the bottom plate fixed. The structures are compressed to 15% nominal strain. Periodic boundary conditions are enforced in the left and right vertical edges of the structure to obtain a periodic response similar to that observed in long sandwich structure configuration. The materials used in the study are defined using an elastoplastic material model and are commonly used in additive manufacturing applications. The material properties taken from the literature are close to the following materials: PC-ABS [51], thermoplastic acetal homopolymer resin [52], and PLA [53]. In Fig. 1a and throughout this paper, orange represents thermoplastic resin, navy represents PC-ABS, and gray represents PLA. Frictional self-contact was defined with a friction coefficient value of 0.4, and structure nodes at the top and bottom plates were allowed to slip horizontally relative to the horizontal rigid plates. The generated mesh was compatible with the periodic boundary conditions, and four-node bilinear elements (CPE4R) with hourglass control and reduced integration were used. Plain-strain condition is assumed to represent a design extruded in the out-of-plane dimension. Hence, out-of-plane buckling is not considered in this study. The workflow to smooth the design boundaries and generate a conformal mesh from a 2D array of design is adopted from the work of [43].

The workflow defined above was used to generate 3314 simulations. All simulations involving physics and finite element analysis were conducted on Delta’s High-Performance Computing (HPC) system hosted at the National Center for Supercomputing Applications (NCSA). The CPU nodes of Delta are equipped with AMD EPYC 7763 Milan CPU cores. On average, each simulation required approximately 232 seconds to complete. Using high throughput computing allowed running up to 12 different FE simulations simultaneously. Hence, the total time required for data generation was 18 hours, corresponding to 216 CPU hours. Four output fields are extracted from the result files at 11 equidistant strain increments up to 15% nominal strain. They are the von Mises stress σ_{vM} , the axial stress σ_{yy} , the strain energy density $g_{se} = \int_0^{\epsilon_f} \boldsymbol{\sigma} : \boldsymbol{\epsilon} d\boldsymbol{\epsilon}$ and the lateral displacement u_x . σ_{vM} is included since it is a commonly used scalar measure for the material stress state, and it is closely related to material yielding. σ_{yy} is included to complement σ_{vM} to indicate whether the material point is under tension or compression. g_{se} is included to further differentiate different materials in different parts of the design. As for the displacements, only u_x is included since the vertical displacement u_y is fixed at the bottom rigid plate locations and does not contain as much information as the former. For simplicity with handling the different FE meshes for different designs, the nodal output fields at the finite element mesh nodes are interpolated to a constant 96×96 pixel grid for all cases. The interpolated fields are stored as 3D arrays each of shape $96 \times 96 \times 4$.

2.2. Neural network framework

This section provides an overview of the neural network (NN) models employed in the proposed framework to generate 2D multi-material designs. As illustrated comprehensively in Fig. 2, the framework consists of two primary components: the Gaussian diffusion model (i.e., a fields generator) that learns to generate field contours based on a target force-displacement curve, and the structure identifier (i.e., two UNet models) that identifies the corresponding multi-material 2D design from the generated fields. Each component plays a crucial role in creating novel designs through generative AI and image segmentation.

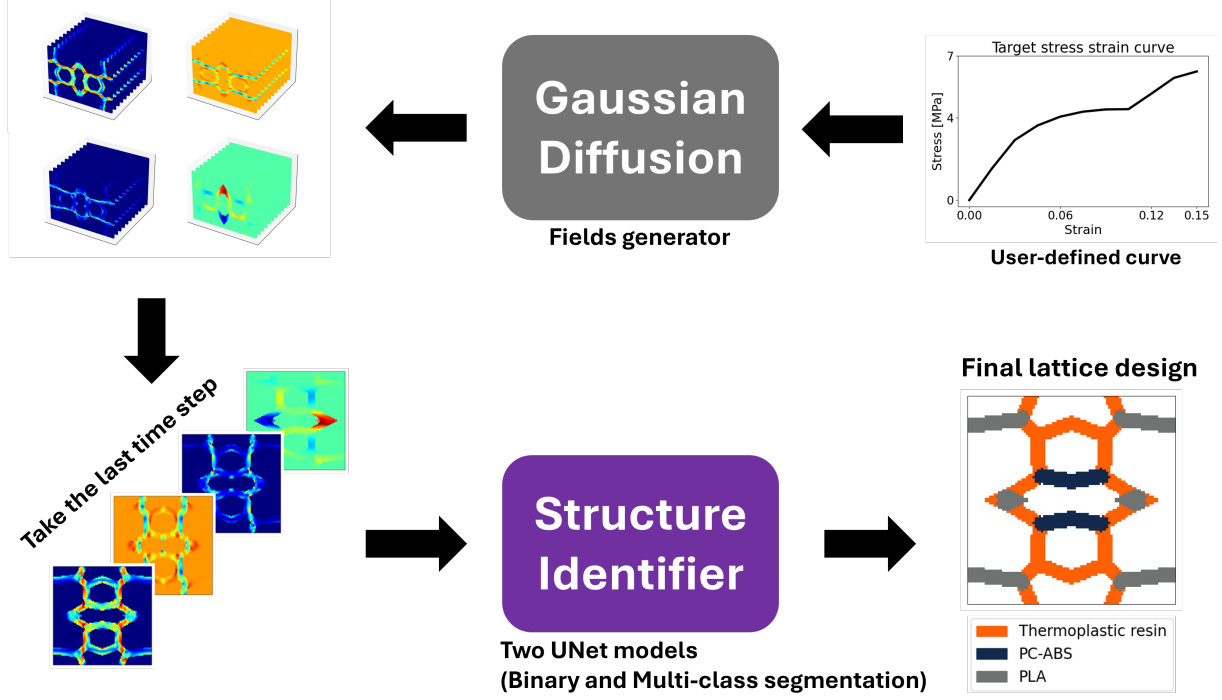


Figure 2: Whole framework on generating a multi-material lattice design from a single stress-strain curve.

2.2.1. Diffusion model as a fields generator

In this work, we adopted a classifier-free guided diffusion model from [43] to generate four mechanical solution fields (i.e., σ_{vM} , σ_{yy} , g_{se} and u_x), based on the user-provided strain-stress curve. This section provides a brief review of the denoising diffusion probabilistic model [28] and the classifier-free guidance method [30] for completeness.

Given a sample \mathbf{x}_0 from a prior data distribution $\mathbf{x}_0 \sim q(\mathbf{x})$, the forward diffusion process of the denoising diffusion probabilistic model adds a small amount of Gaussian noise to the sample over T steps. This results in a sequence of samples $\mathbf{x}_1, \mathbf{x}_2, \dots, \mathbf{x}_T$. Each step in the diffusion process is controlled by a variance schedule $\{\beta_t \in (0, 1)\}_{t=1}^T$,

$$q(\mathbf{x}_t | \mathbf{x}_{t-1}) = \mathcal{N}(\mathbf{x}_t; \sqrt{1 - \beta_t} \mathbf{x}_{t-1}, \beta_t \mathbf{I}), \quad (1a)$$

$$q(\mathbf{x}_{1:T} | \mathbf{x}_0) = \prod_{t=1}^T q(\mathbf{x}_t | \mathbf{x}_{t-1}). \quad (1b)$$

The sample \mathbf{x}_0 gradually loses its features and eventually becomes an isotropic Gaussian distribution for large T . This diffusion process has the elegant property that we can sample \mathbf{x}_t at any time step t using the reparametrization trick,

$$\mathbf{x}_t = \sqrt{\bar{\alpha}_t} \mathbf{x}_0 + \sqrt{1 - \bar{\alpha}_t} \epsilon_t, \quad (2a)$$

$$q(\mathbf{x}_t | \mathbf{x}_0) = \mathcal{N}(\mathbf{x}_t; \sqrt{\bar{\alpha}_t} \mathbf{x}_0, (1 - \bar{\alpha}_t) \mathbf{I}), \quad (2b)$$

where $\alpha_t = 1 - \beta_t$, $\bar{\alpha}_t = \prod_{i=1}^t \alpha_i$, and $\epsilon_t \sim \mathcal{N}(0, \mathbf{I})$.

By reversing the diffusion process, we can sample from $q(\mathbf{x}_{t-1}|\mathbf{x}_t, \mathbf{x}_0)$ and ultimately generate the true sample \mathbf{x}_0 from Gaussian noise $\mathbf{x}_T \sim \mathcal{N}(0, \mathbf{I})$. Using Bayesian rule, the reverse posterior distribution conditioned on \mathbf{x}_0 is traced,

$$q(\mathbf{x}_{t-1}|\mathbf{x}_t, \mathbf{x}_0) = \mathcal{N}\left(\mathbf{x}_{t-1}; \tilde{\boldsymbol{\mu}}_t(\mathbf{x}_t, \mathbf{x}_0), \tilde{\beta}_t \mathbf{I}\right), \quad (3)$$

where $\tilde{\boldsymbol{\mu}}_t(\mathbf{x}_t, \mathbf{x}_0) = \frac{1}{\sqrt{\alpha_t}} \left(\mathbf{x}_t - \frac{1-\alpha_t}{\sqrt{1-\bar{\alpha}_t}} \epsilon_t \right)$ and $\tilde{\beta}_t = \frac{1-\bar{\alpha}_{t-1}}{1-\bar{\alpha}_t} \beta_t$.

In a real generative process, we cannot directly evaluate $q(\mathbf{x}_{t-1}|\mathbf{x}_t, \mathbf{x}_0)$ because it requires the entire training samples and the diffusion noise dataset. Instead, we propose a posterior distribution $p_\theta(\mathbf{x}_{t-1}|\mathbf{x}_t)$ to approximate the true posterior distribution $q(\mathbf{x}_{t-1}|\mathbf{x}_t, \mathbf{x}_0)$,

$$p_\theta(\mathbf{x}_{t-1}|\mathbf{x}_t) = \mathcal{N}(\mathbf{x}_{t-1}; \boldsymbol{\mu}_\theta(\mathbf{x}_t, t), \boldsymbol{\Sigma}_\theta(\mathbf{x}_t, t)), \quad (4)$$

The reverse denoising process is then controlled by,

$$p_\theta(\mathbf{x}_{0:T}) = p(\mathbf{x}_T) \prod_{t=1}^T p_\theta(\mathbf{x}_{t-1}|\mathbf{x}_t), \quad (5)$$

where $\boldsymbol{\Sigma}_\theta(\mathbf{x}_t, t)$ is the same as $\tilde{\beta}_t \mathbf{I}$, and $\boldsymbol{\mu}_\theta(\mathbf{x}_t, t)$ has the same form as $\tilde{\boldsymbol{\mu}}_t(\mathbf{x}_t, \mathbf{x}_0)$ but with learnable parameters θ ,

$$\boldsymbol{\mu}_\theta(\mathbf{x}_t, t) = \frac{1}{\sqrt{\alpha_t}} \left(\mathbf{x}_t - \frac{1-\alpha_t}{\sqrt{1-\bar{\alpha}_t}} \epsilon_\theta(\mathbf{x}_t, t) \right). \quad (6)$$

The optimization objective of the denoising diffusion probabilistic model is to maximize the log-likelihood $\log p_\theta(\mathbf{x}_{0:T})$, which results in the following loss function,

$$L = |\epsilon_\theta(\mathbf{x}_t, t) - \epsilon_t(\mathbf{x}_t, t)|. \quad (7)$$

Training a NN $\epsilon_\theta(\mathbf{x}_t, t)$ and minimizing the loss function L leads to $\boldsymbol{\mu}_\theta(\mathbf{x}_t, t) \approx \tilde{\boldsymbol{\mu}}_t(\mathbf{x}_t, \mathbf{x}_0)$, thus making the proposed posterior distribution $p_\theta(\mathbf{x}_{t-1}|\mathbf{x}_t)$ close to the true posterior distribution $q(\mathbf{x}_{t-1}|\mathbf{x}_t, \mathbf{x}_0)$.

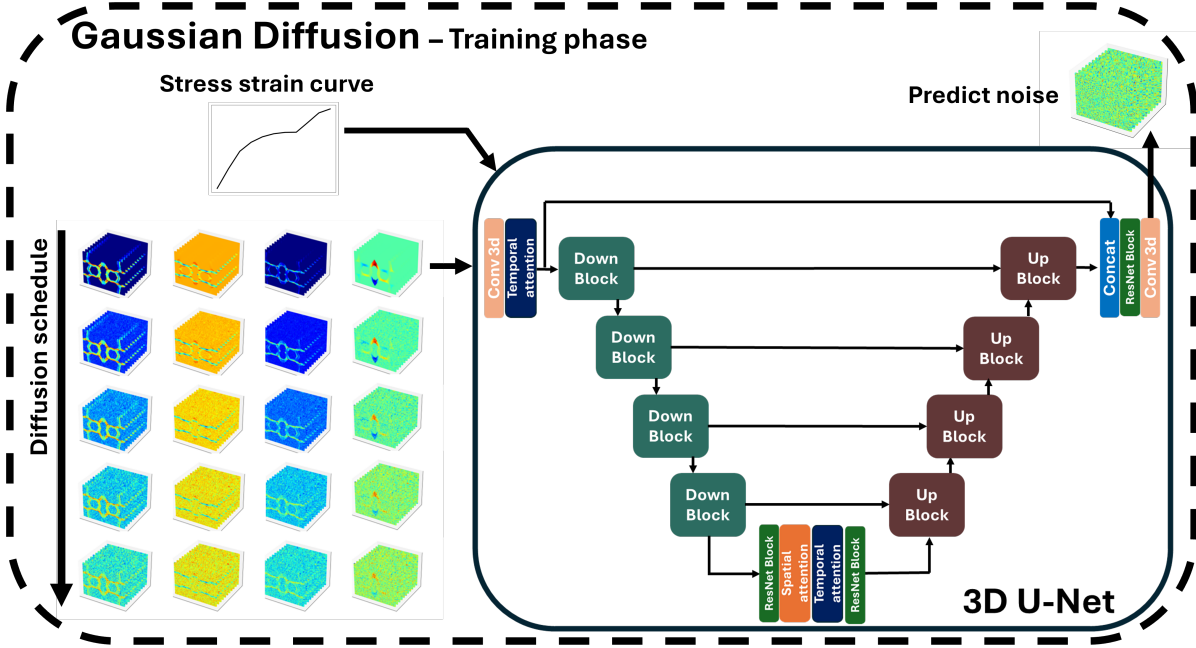
The above reverse generative process is random and not controlled by any specific target. In specific design tasks, we aim to generate fields that represent the target, such as the force-displacement curve, which requires training the NN $\epsilon_\theta(\mathbf{x}_t, t)$ with conditional information. To incorporate the condition information \mathbf{y} into the diffusion process, Ho and Salimans [30] proposed a classifier-free guidance method without an explicit classifier [29], incorporating the scores from a conditional diffusion model $p_\theta(\mathbf{x}|\mathbf{c})$ and an unconditional diffusion model $p_\theta(\mathbf{x})$. The noise estimators $\epsilon_\theta(\mathbf{x}_t, t)$ of $p_\theta(\mathbf{x})$ and $\epsilon_\theta(\mathbf{x}_t, t, \mathbf{c} = \mathbf{y})$ of $p_\theta(\mathbf{x}|\mathbf{c})$ are trained in a single NN $\epsilon_\theta(\mathbf{x}_t, t, \mathbf{c})$. Here, $\epsilon_\theta(\mathbf{x}_t, t, \mathbf{c} = \mathbf{y})$ is trained with paired data $(\mathbf{x}, \mathbf{c} = \mathbf{y})$, and $\epsilon_\theta(\mathbf{x}_t, t)$ is trained with data \mathbf{x} only, i.e., $(\mathbf{x}, \mathbf{c} = \emptyset)$. During the training process, the condition information \mathbf{c} is randomly set as $\mathbf{c} = \emptyset$ or $\mathbf{c} = \mathbf{y}$ for sample (\mathbf{x}, \mathbf{y}) at different time steps t , allowing the model to learn to generate fields both conditionally and unconditionally. During the reverse inference process, ϵ_θ in Eq. (6) is replaced by the linear summation of conditional and unconditional noise estimators,

$$\epsilon_\theta(\mathbf{x}_t, t, \mathbf{c}) = (1+w)\epsilon_\theta(\mathbf{x}_t, t, \mathbf{c} = \mathbf{y}) - w\epsilon_\theta(\mathbf{x}_t, t, \mathbf{c} = \emptyset), \quad (8)$$

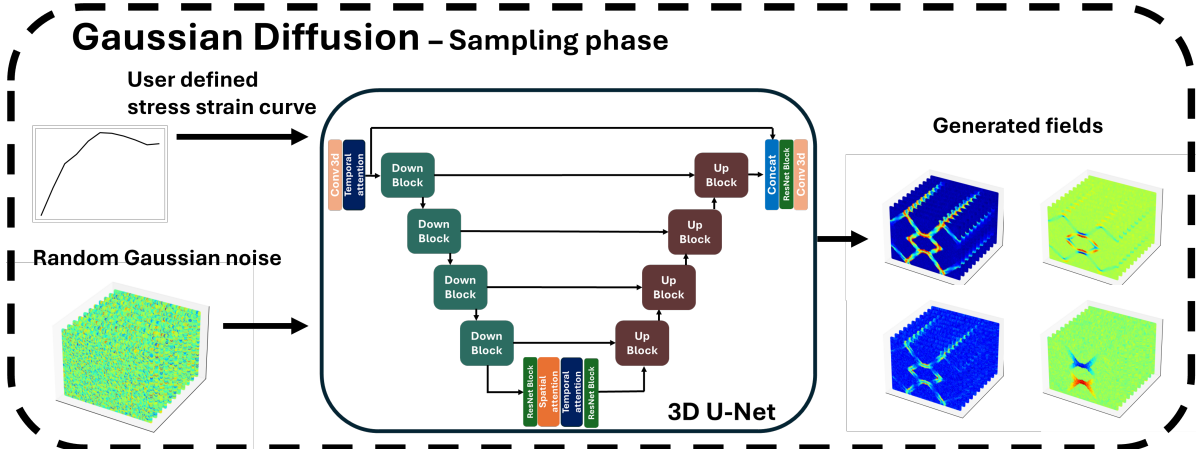
where $w \geq 0$ is the guidance weight.



(a) Down and Up blocks used in the Gaussian diffusion model



(b) Training phase of the Gaussian diffusion model. 3D UNet serves a key algorithm for predicting noise added to each step in the diffusion process.



(c) Sampling phase of the Gaussian diffusion model. Trained 3D UNet takes the random Gaussian noise and user-defined target curve as an input, then serves role of a denoising algorithm to generate fields from the given random noise.

Figure 3: Architecture of the Gaussian diffusion model: Down and Up blocks used in the 3D UNet, and overall structure of the diffusion process with 3D UNet as the core noise prediction algorithm

The classifier-free guided diffusion model predicts these solution fields by iteratively denoising random noise inputs, resulting in multiple sets of 2D field values, representing field values for each time step that serves as the basis for subsequent design structure identification. A 3D UNet architecture was integrated with the Gaussian Diffusion model, serving as the core model for the generative process due to its ability to handle multiple 2D images as a time sequence. Given the spatial and temporal information embedded in the data, spatial linear self-attention and temporal self-attention mechanisms were incorporated with ResNet blocks within each encoder and decoder block of the 3D UNet. Each attention block contains 8 attention heads. The network structure includes four upsampling and downsampling encoder-decoder blocks, resulting in a total depth of five, including the input layer. Schematics of the encoding and decoding blocks used in the model are shown in Fig. 3a. To handle temporal strain steps, which consist of 11 stress values, a linear layer was employed to convert these steps into a token embedding vector.

Fig. 3b illustrates the training phase of the model. The structure is based on a forward diffusion process, where a given design is gradually corrupted by adding Gaussian noise over a series of time steps. A 3D UNet plays a crucial role in predicting the noise added at each step. The model learns to reverse this process, iteratively denoising the input to recover the original design. The sampling phase, depicted in Fig. 3c, begins with pure noise and processes the reverse Markov chain to achieve our goal: obtaining 2D field values at each time step. This process is governed by the same noise schedule used in training but applied in reverse order.

2.2.2. Two UNets as a structure identifier

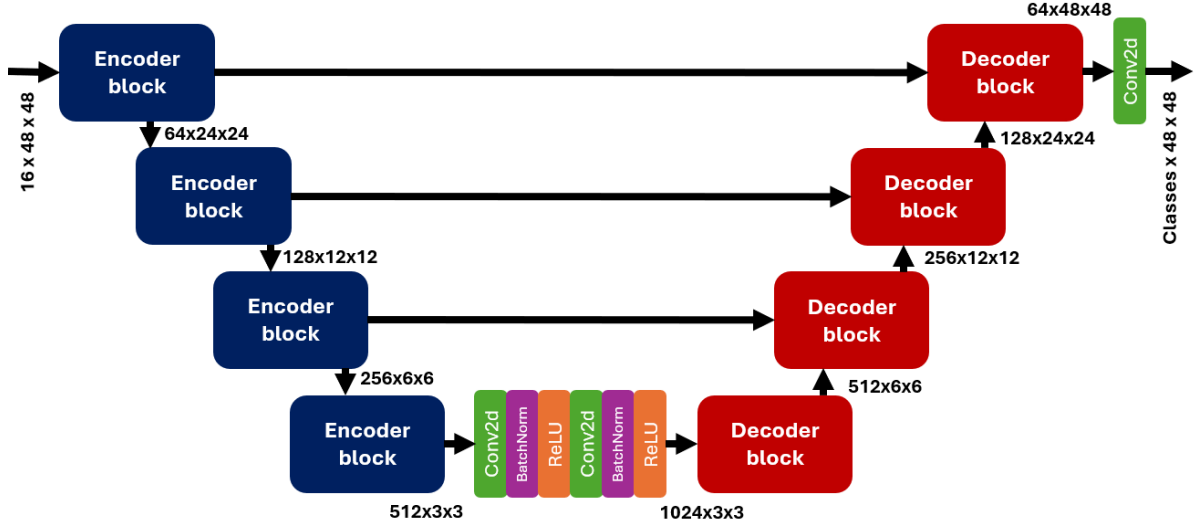
Similar to the work of [43], the diffusion model generates mechanical solution fields instead of the desired design directly. In addition, due to the stochastic nature of the diffusion process, these raw outputs may contain noise and other imperfections that need to be properly addressed to obtain a physically valid structure. A simple stress threshold is used in [43] to identify the void and solid regions for a single material. This would not work for a multi-material scenario such as the one considered in this work. Therefore, in this work, we proposed to use two consecutive UNets to post-process the fields generated by the diffusion model to obtain the final design: the first one performs a binary segmentation to identify solid and void regions, and the other one performs a multi-class segmentation to identify the material distribution within the solid region. This two-step structure identification process ensures that the final designs are coherent with the designs created initially during the training data generation phase and renders the structure identification process more explainable.

The first UNet is designed to perform a binary segmentation on the output fields from the diffusion model. We used the last time step of the Gaussian diffusion outputs from each channel as a training data, since the fields at this final step show the most distinct contrast with void regions. Then it (i.e., the mechanical fields obtained from simulations) was augmented by randomly selecting one in the following list: Random horizontal flip, Random vertical flip, Random rotation by 90 degrees, and Gaussian blur. With data augmentation, the training data was expanded 6 times of its original size to enhance generalizability. To enhance resistance of the model to the inherent noise in the diffusion-predicted field contours, random Gaussian noises were added to the training data field values to resemble the noisy diffusion-generated output, as the diffusion algorithm iteratively adds Gaussian noise in its training phase. Finally, to ensure symmetry in the design, each full-field data (of shape 96×96) was divided into four symmetric parts, four 48×48 images, and stacked along the channel axis. Each part was rotated and flipped to match the orientation of the upper-left slice

when stacking. As a result, the channel axis became four times larger than before. The augmented-then-noise-enhanced dataset is used in the training of both UNet models in the structure identifier. The binary segmentation UNet employs an encoder-decoder structure that processes the input to distinguish between material and void regions. The encoder and decoder blocks are constructed out of multiple layers of computation as Fig. 4a and the binary cross entropy loss were used as a loss function. The output from this structure is a binary image with pixels of 48×48 , where the material regions are identified against the void background. A schematic of the UNet architecture is shown in Fig. 4b.



(a) Encoder and decoder block structure for the UNets used



(b) Single UNet architecture used in the structure identifier. The 1st and 2nd UNets share this structure, differing only in the number of output classes.

Figure 4: Block structure and overall architecture of the UNet-based structure identifier

After the initial binary segmentation to differentiate solid and void regions, a second UNet now undertakes the task of multi-class segmentation to obtain the final multi-material design. The training data pre-treated with data augmentation and added noise are used in the training of this second UNet, except that now the fields in the void region (predicted from the first UNet) are set to 0 before training. This additional treatment step ensures that the second UNet can easily segment out void pixels and concentrate more effectively on the material pixels to perform the material classification task. The architecture follows an encoder-decoder structure similar to that of the first

UNet, but with modifications in the final layer to classify each pixel into specific material classes. Since there are 3 materials and a void to classify for each pixels, channel of 4 was set to be the output from the second UNet. The main difference from the first UNet lies in the loss function, where we use the DiceCE loss defined as:

$$\begin{aligned}\mathcal{L}_{\text{DiceCE}} &= \mathcal{L}_{\text{Dice}} + \mathcal{L}_{\text{CE}}, \\ \mathcal{L}_{\text{Dice}} &= \frac{1}{C} \sum_{c=1}^C \left(1 - \frac{2 \sum_{i=1}^N y_{i,c} \sigma(z_{i,c}) + \epsilon}{\sum_{i=1}^N y_{i,c} + \sum_{i=1}^N \sigma(z_{i,c}) + \epsilon} \right), \\ \mathcal{L}_{\text{CE}} &= -\frac{1}{N} \sum_{i=1}^N \sum_{c=1}^C y_{i,c} \log p_{i,c}, \quad p_{i,c} = \frac{\exp(z_{i,c})}{\sum_{j=1}^C \exp(z_{i,j})}.\end{aligned}\tag{9}$$

This loss function is a sum of both the Dice loss and the cross-entropy loss. In Eq. (9), C denotes the total number of classes, N represents the number of pixels in one image, $y_{i,c}$ is the one-hot encoded true label for pixel i and channel c , $z_{i,c}$ is the output logit for pixel i and channel c , σ is the sigmoid function, and ϵ is a small constant added to prevent division by zero.

The outputs from this network is a 48×48 image, each pixel segmented as one of the four possible classes (including void). A schematic of this UNet is the same with the first UNet figure as shown in Fig. 4b. The raw mechanical fields in the training dataset and predicted by the diffusion model are 96×96 images, while both UNet models operate on 48×48 images. This choice is deliberate since we would like the full designs (have shape 96×96) to be periodic and symmetric, which can be achieved exactly by copying and flipping the one-quarter design (i.e., the 48×48 image). As such, each input field are first sliced into 4 quarters and rotated to a consistent orientation, turning each 96×96 input image into shape $48 \times 48 \times 4$. The complete workflow for lattice structure generation given a user-defined stress-strain curve is shown in Fig. 5.

3. Results and discussion

3.1. Diffusion outputs and their noisy nature

To evaluate the diffusion model's performance across various mechanical behaviors, nine diverse stress-strain curves were selected from finite element simulation results. These curves, shown in Fig. 6, serve as target behaviors for the framework to reproduce similar designs. Curves 1 and 5 exhibit conventional elasto-plastic behavior with distinct elastic and plastic regions, including strain hardening and softening. Curve 2 displays a significant plateau in the plastic region, indicative of perfect plasticity or a prolonged yielding phase. Curve 3 mirrors the behavior of Curve 2 but at a five-times higher magnitude, testing the framework's ability to scale behaviors. Curves 4 and 9 feature abrupt stress jumps, indicating densification of the structure at larger strains. Curve 6 demonstrates monotonic hardening throughout the strain range, a behavior seen in some composite materials or during certain thermomechanical processes. Curve 7 presents a complex response with two distinct slopes separated by a plateau, potentially representing a material with multiple deformation mechanisms or phase changes. Lastly, Curve 8 showcases a pronounced stress decrease after reaching a maximum, typical of materials exhibiting significant softening due to buckling or fracture. This diverse set of target curves encompasses a wide range of mechanical responses, challenging the framework to reproduce behaviors from conventional plasticity to more complex, non-linear phenomena. Such variety ensures a robust evaluation of the framework's capabilities in mimicking realistic material behaviors.

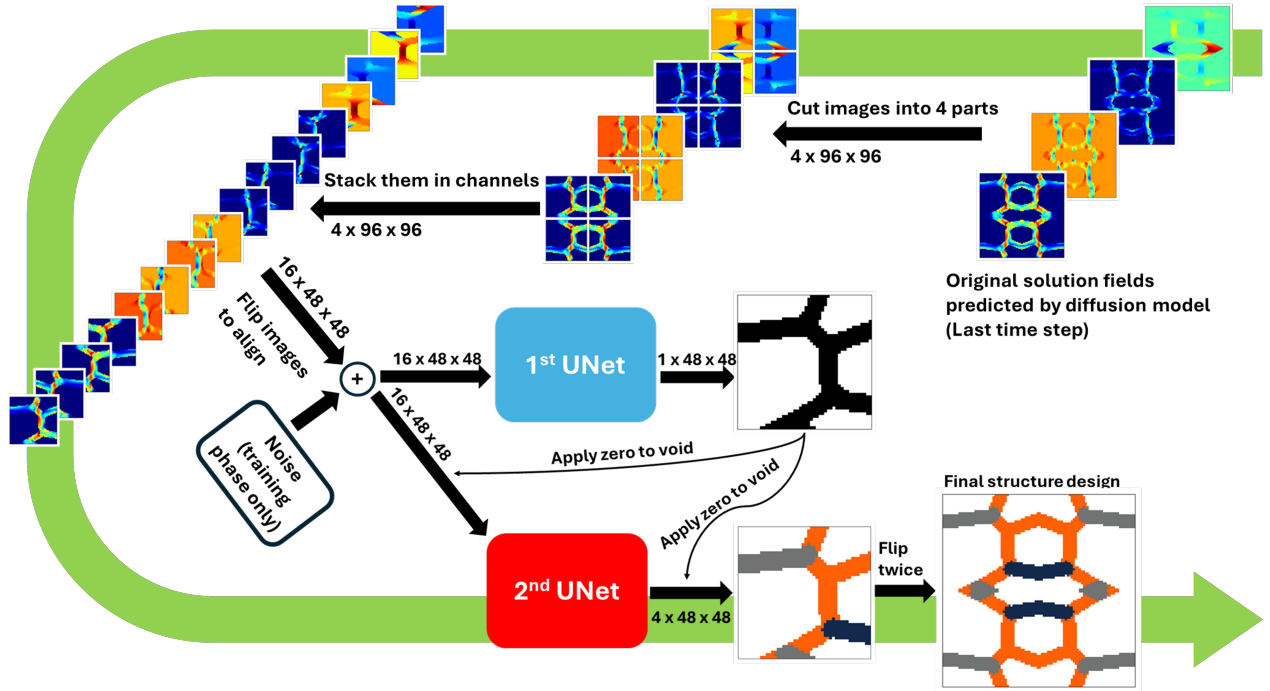


Figure 5: Two UNets after diffusion model as a structure identifier

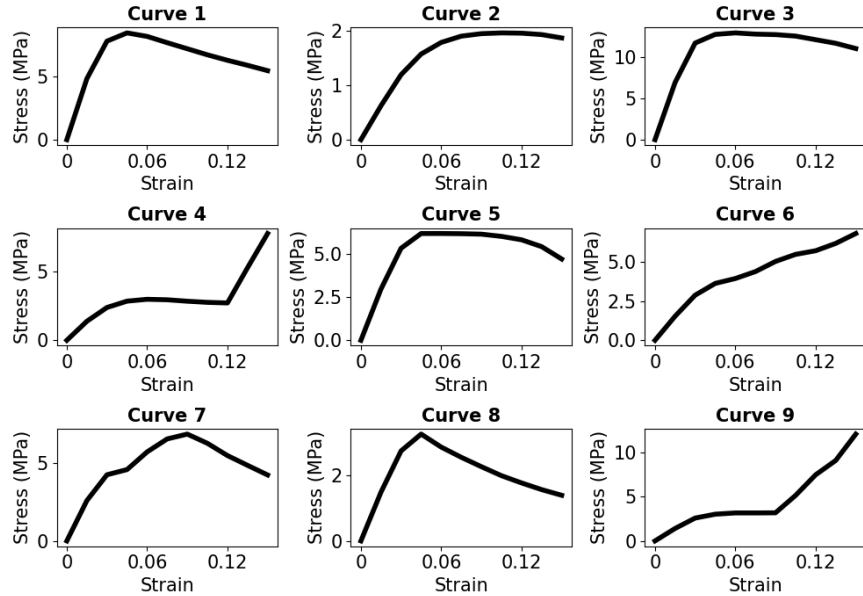


Figure 6: Nine target curves chosen for the diffusion model to mimic.

The diffusion model was trained over 180,000 iterations with 3314 simulations. The training process underwent 21 hours to complete, and the following sampling process took approximately 4 hours to generate 450 samples. Fig. 7 presents an illustrative example of the raw output generated by the diffusion model, using the target curves in Fig. 6. Consistent with its training paradigm, the model produces four distinct fields for each sample. A prominent characteristic of these outputs is the presence of Gaussian noise, a consequence of the model's inherently stochastic nature. While

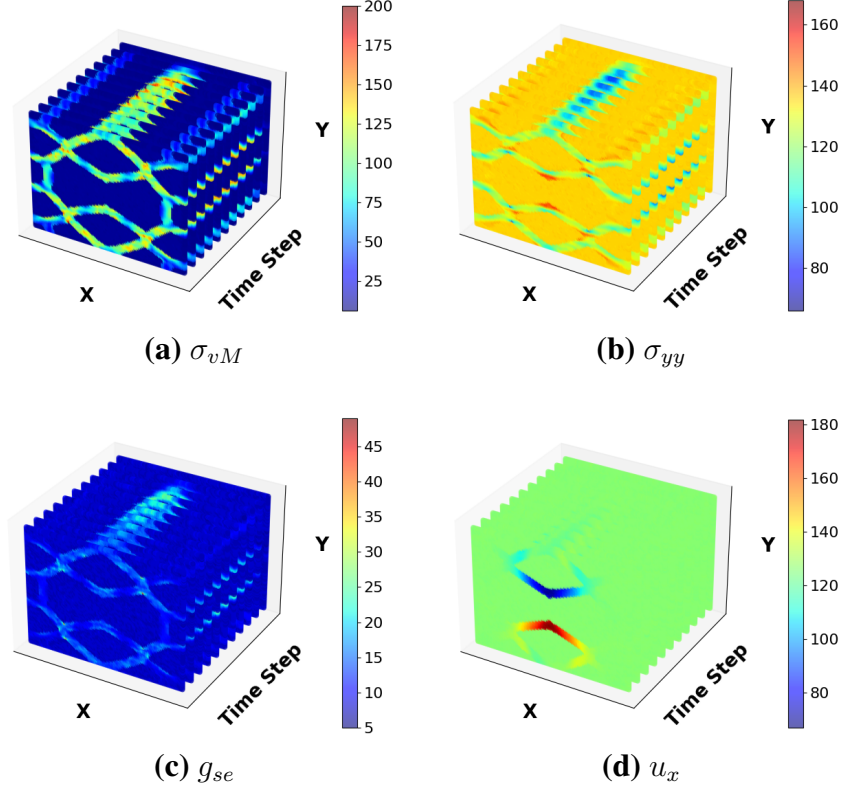
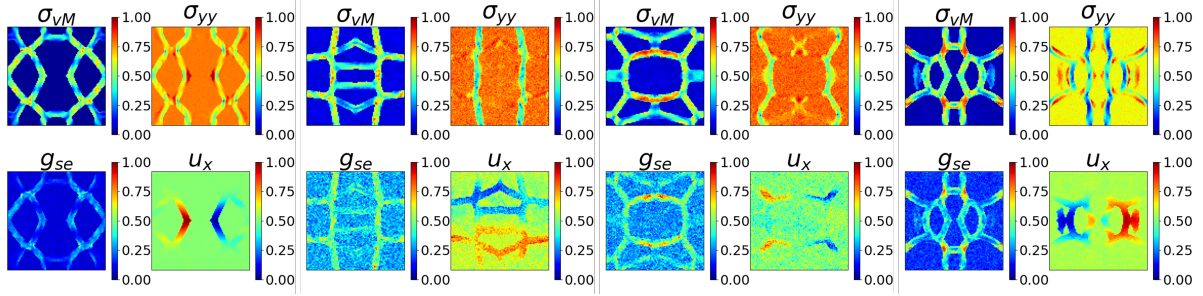


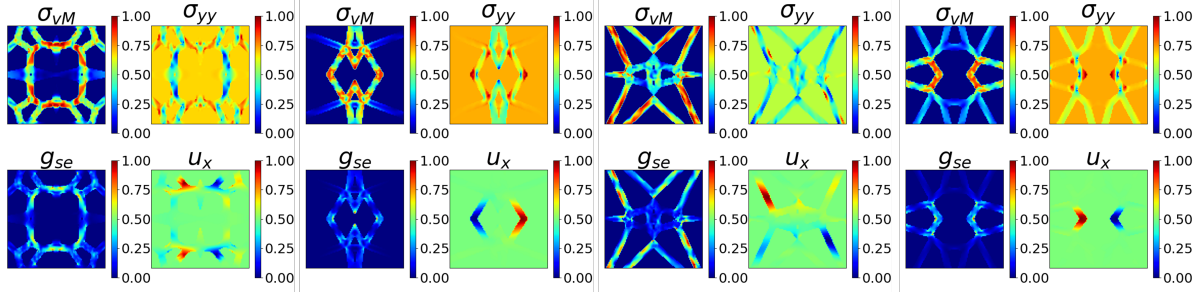
Figure 7: Diffusion raw output for a single sample with 11 time steps in each of the 4 fields.

the iterative denoising process within the diffusion model aims to mitigate artifacts and eliminate noise, the raw output often retains residual noise. This noise can impede the structure identifier’s ability to accurately discern the lattice design. For example, Fig. 8 illustrates the contrast in noise levels between diffusion model outputs and FEA for the last time step. The figure presents two sets of normalized samples: Fig. 8a shows outputs from the diffusion model, while Fig. 8b displays results from FEA. Visual inspection reveals that the fields generated by the diffusion model exhibit significantly more granularity compared to the smoother, cleaner outputs obtained from FEA. This disparity in image quality underscores the challenges posed by the noise in diffusion model outputs and highlights the need for strategies in countering the residual noise in the prediction for practical applications.

To characterize the noise level in the diffusion-generated data, several metrics can be employed to quantify noise within a single image. Typically, measuring noise in an image requires two versions: an original and a noisy version of the same image. However, in our work, there are no “original” versions for the diffusion-generated data, as these images are newly created. Therefore, a noise measure that can be computed using just one image is necessary. Discrete cosine transform (DCT) energy [54] was utilized in this work to evaluate a noise in a single image. The DCT energy is obtained by transforming an image using the DCT and summing the absolute values of the transformed pixel values. Since this measure can represent the frequency content of an image, a noise-free image will result low DCT energy value due to its lower-frequency components. Conversely, a noisy image will result a high DCT energy value because noise typically spreads across higher frequencies.

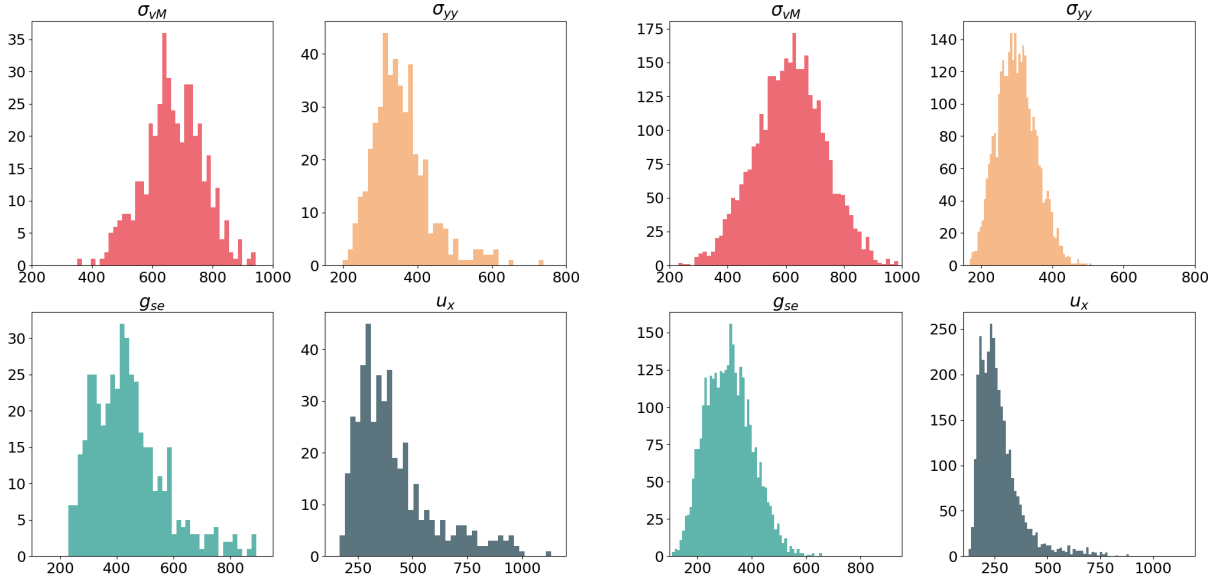


(a) Normalized raw field output from diffusion model, last time step



(b) Normalized fields extracted from FEA, last time step

Figure 8: Visual noise comparison of field values obtained from diffusion model and FEA.



(a) DCT energy of diffusion model output

(b) DCT energy of FEA fields

Figure 9: Histograms of DCT energy for each field property, last time step in the two datasets: (a) diffusion model outputs and (b) FEA. The DCT energy metrics were computed for individual field properties to compare the noise characteristics between the datasets.

Fig. 9 compares the DCT energy of the last time step between the diffusion model output and the FEA. It can be observed that the DCT energy values in the diffusion-generated data are generally

higher across all four fields, indicating that these data contain more high-frequency components, which are likely attributed to noise. Additionally, while the DCT energy histogram for σ_{vM} shows little difference between the two datasets, the g_{se} and u_x fields exhibit more significant differences. The corresponding statistics are summarized in Table 1. In terms of mean values, the DCT energy for σ_{vM} is 9% higher in the diffusion model output compared to the FEA fields. For the σ_{yy} field, it is 18% higher, for the g_{se} field, it is 38% higher, and for the u_x field, it is 52% higher in the diffusion outputs.

Table 1: DCT Energy Statistics for Both Datasets: Diffusion Generated and FEA, last time step

Diffusion Generated			FEA		
Channel	Mean	Maximum	Channel	Mean	Maximum
σ_{vM}	671	943	σ_{vM}	615	1070
σ_{yy}	354	739	σ_{yy}	300	510
g_{se}	440	891	g_{se}	319	658
u_x	415	1130	u_x	272	887

The residual noise within the diffusion output manifests in various ways, influenced by factors such as the lattice structure’s complexity and the intrinsic characteristics of the simulated mechanical fields. Traditional denoising algorithms, like Gaussian filters or Block-Matching and 3D Filtering (BM3D), offer a potential solution for refining noisy raw outputs. These methods are computationally efficient and straightforward to implement. However, our approach leverages separate NNs in conjunction with the diffusion model to refine and identify the multi-material design. To implement this strategy, Gaussian noise was artificially introduced to the FEA training data (training dataset of diffusion model). The NNs described in Section 2.2.2 were subsequently trained on this noise-enhanced data. This approach allows the networks to effectively handle the noisy raw outputs of the diffusion model during inference, as they have been conditioned on similarly noisy data during training. It is crucial that the noise characteristics added to the FEA training data comprehensively represent those present in the diffusion outputs. We selected Gaussian noise to align with the noise type used in the diffusion model. The intensity of the noise introduced to the training data was calibrated to match the highest noise levels observed in the diffusion outputs, as measured by their DCT energy. Specifically, the Gaussian noise was added to the FEA simulation data such that the maximum DCT energy values exceed at least with 25.0% margin to those of the diffusion-generated last time step outputs for each field separately. For example, the DCT energy for σ_{vM} in the noise-enhanced FEA training data was set at 125% of the maximum value found in the diffusion-generated σ_{vM} fields. Similarly, the fields σ_{yy} , g_{se} , and u_x in the FEA training data were also augmented with Gaussian noise to reach 125% of the respective maximum DCT energy levels of the diffusion-generated fields. This approach ensures that the structure identifier was trained on even noisier data than it would encounter during inference, preparing it to handle diffusion-generated fields effectively in the inference phase.

Table 2 summarizes the DCT energy statistics of the noise-enhanced FEA training data. The last column in this table (i.e., Max DCT Energy Ratio Noise-enhanced / Diffusion), provides a comparison between the noise-enhanced FEA simulations and the raw diffusion outputs. This ratio, consistently exceeding 100% for all channels, demonstrates that our noise-enhanced training

dataset indeed incorporates noisier data than the raw diffusion outputs. Specifically, the maximum DCT energy ratios range from 125% to 127% across all channels. This indicates that we have successfully introduced an additional 25.0% noise (or even more) margin in our training data compared to the expected noise levels in the diffusion outputs. The step ensures that the NNs are trained on data with a higher noise level, improving their robustness and effectiveness when handling the noisy outputs of the diffusion model during the inference phase.

Table 2: DCT Energy Statistics for Noise added FEA simulation, last time step

Noise added FEA Simulations			
Channel	Mean	Maximum	Max DCT Energy Ratio (Noise-enhanced FEA / Diffusion)
σ_{vM}	807	1190	127%
σ_{yy}	802	934	126%
g_{se}	856	1120	125%
u_x	1160	1420	125%

Fig. 10 illustrates four samples in the noise-enhanced FEA training data. Visually, they resemble Fig. 9a more closely than Fig. 9b, which aligns with our intention to simulate the noise characteristics of the diffusion model outputs. The added Gaussian noise introduces a granular texture to the images, mimicking the stochastic nature of diffusion-generated samples. This visual similarity is crucial, as the structure identifier consists of convolutional layers and learn directly from images in the training data. The figure also indicates that our noise-enhancement strategy successfully bridges the gap between the clean FEA and the noisier diffusion outputs.

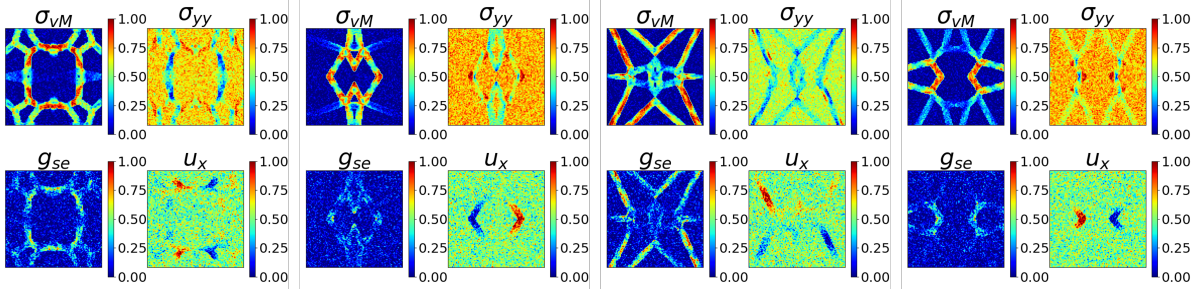


Figure 10: Four samples in the noise-enhanced FEA training data. Each sample contains 4 fields: σ_{vM} , σ_{yy} , g_{se} , and u_x . For comparison, same samples with Fig. 8b were taken, but with added noise.

3.2. Performance of the structure identifier

The structure identifier (i.e., two UNets) were trained and evaluated using an 90-10 split of the dataset into training and test sets. From the 3314 simulations, 332 samples were randomly selected to form the test dataset. The training process consisted up to 500 epochs with stopping early if the test accuracy reaches 99.9%. NN training was executed on an Nvidia A100 GPU. The first UNet took 47 minutes with 53 epochs resulting in an average iteration time of 52.8 seconds, and the second UNet took 3 hours with 178 epochs, having 62.4 seconds on average per iteration.

To evaluate the accuracy of the trained NNs, the following metrics were employed:

$$\begin{aligned}
\text{Accuracy}(\%) &= \frac{\sum_{p=1}^M \sum_{q=1}^M \mathbb{1}(\mathbf{Y}_{\text{true},p,q} = \mathbf{Y}_{\text{pred},p,q})}{M^2} \times 100(\%), \\
\text{Weighted DSC}(\%) &= \left(\sum_{j=1}^C w_j \cdot \text{DSC}_j \right) \times 100(\%), \\
\text{DSC}_j &= \begin{cases} \frac{2|\mathbf{Y}_{\text{true}}^j \cap \mathbf{Y}_{\text{pred}}^j|}{|\mathbf{Y}_{\text{true}}^j| + |\mathbf{Y}_{\text{pred}}^j|} & \text{if } |\mathbf{Y}_{\text{true}}^j| + |\mathbf{Y}_{\text{pred}}^j| > 0 \\ 1 & \text{if } |\mathbf{Y}_{\text{true}}^j| + |\mathbf{Y}_{\text{pred}}^j| = 0 \end{cases}, \quad w_j = \frac{|\mathbf{Y}_{\text{true}}^j|}{\sum_{k=1}^C |\mathbf{Y}_{\text{true}}^k|}
\end{aligned} \tag{10}$$

where $M \times M$ is the size of each 2D design image, $\mathbb{1}$ is the indicator function which returns 1 if the condition is true and 0 otherwise. \mathbf{Y}_{true} , \mathbf{Y}_{pred} are true and predicted images respectively. The (p, q) subscript in the first equation denotes (p, q) -pixel value in \mathbf{Y}_{true} and \mathbf{Y}_{pred} . In the second equation, C is the number of classes, w_j is the weight assigned to class j . This weight is calculated as the ratio of the number of pixels belonging to class j in the true segmentation map \mathbf{y}_{true} to the total number of pixels in all classes. Similarly, DSC_j represents the Dice Similarity Coefficient (DSC) for class j , obtained from the third row of Eq. (10). The numerator represents two times the intersection of the true and predicted segmentation for class j (denoted as $\mathbf{Y}_{\text{true}}^j$ and $\mathbf{Y}_{\text{pred}}^j$), and the denominator is the total number of pixels labeled as class j in both the ground truth and the predicted segmentation. The accuracy and weighted DSC metrics offer a thorough assessment of the model's performance in predicting both material mask and multi-material design, by a quantitative comparison between the NN's predictions and the ground truth data from the design itself. The DSC equation was modified to encompass multi-class case, calculating weighted DSC values for each class and averaging them.

With the early-stopping mechanism employed, both UNet models did not require the full 500 epochs to achieve 99.9% accuracy. The first UNet, tasked with binary segmentation, reached the target accuracy of 99.9% after 53 epochs. The second UNet, responsible for multi-class segmentation, achieved the same target accuracy after 178 epochs. The test dataset results demonstrate that the structure identification architecture attained a consistently high accuracy in predicting designs based on their mechanical fields, effectively extracting designs from the noisy raw outputs of the diffusion model. The following Table 3 provides a detailed overview of the performance metrics, as defined in Eq. (10), for the two UNets within the structure identifier model across various percentiles, including the best case, 25th percentile, 50th percentile (median), 75th percentile, and the worst-case scenario. The results demonstrate that the structure identifier exhibits robust performance on the test dataset, which notably contains samples with noise levels exceeding those anticipated in the inference data.

Using the trained model, an inference process was conducted on the raw output from the diffusion model to obtain the 2D multi-material designs. Given the stochastic nature of input noise image to the diffusion model, 50 designs were generated from each target curve, leading to a total of 450 designs. Fig. 11 shows 5 randomly selected multi-material designs for each target curve, showing the diversity of the designs generated from the current framework.

3.3. FEA validation of designs produced by NNs

Ensuring that these designs are manufacturable and closely resemble the initial Voronoi designs used during the training data generation phase is crucial. To evaluate the manufacturability

Table 3: Structure identifier performance metrics

UNet-1: binary	Best	25 th	50 th	75 th	Worst
Accuracy	100%	100%	100%	99.9%	98.6%
Weighted DSC	100%	100%	100%	99.9%	99.5%

UNet-2: multi-class	Best	25 th	50 th	75 th	Worst
Accuracy	100%	100%	99.9%	99.9%	99.5%
Weighted DSC	100%	99.9%	99.9%	99.9%	99.5%

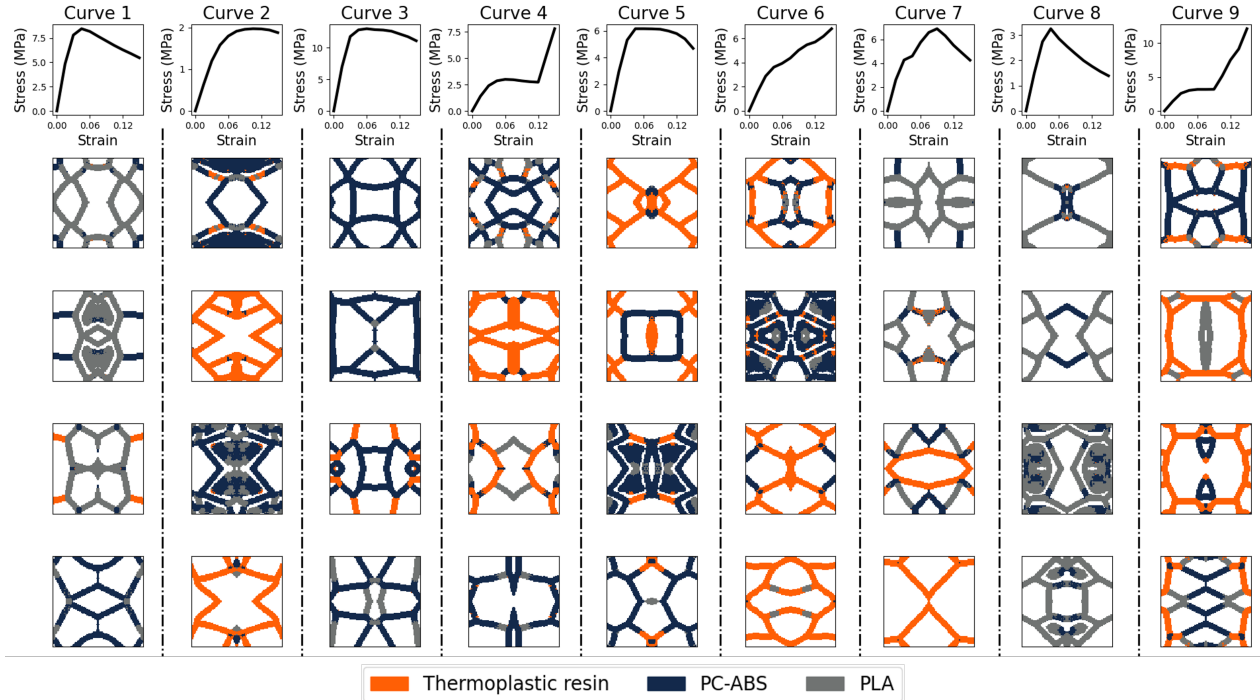


Figure 11: Designs created by NNs corresponding to the target curve at the first row. Five were chosen randomly out of 50 designs generated for each target curve.

and plausibility of designs generated by the diffusion and structure identifier framework, we conducted the finite element analysis identical to that described in Section 2.1. The FEA results, particularly the stress-strain curves, were compared against the original target curves used to guide the diffusion model. For each target curve, 50 designs were generated, resulting in 50 corresponding stress-strain curves from FEA. The similarity between these generated curves and the target curve was assessed to gauge the effectiveness of the generative AI model in inherently mimicking the desired mechanical properties. To quantify the closeness between the generated design curves and their corresponding target curves, we employed the metrics detailed in Eq. (11). Let y_{true} and y_{pred} represent the target curve and the curves from generated designs, respectively, and S denote the number of points in both curves. As defined in Eq. (11), we utilized the Relative Root Mean Squared Error (RRMSE) and the Relative Mean Absolute Error (RMAE) to provide a comprehensive analysis of the curve similarities. This approach allowed us to objectively as-

sess the performance of our generative model in producing designs that closely match the desired mechanical properties specified by the target curves.

$$\begin{aligned} \text{RRMSE}(\%) &= \frac{\|y_{true} - y_{pred}\|_2}{\|y_{true}\|_2} \times 100(\%) \\ \text{RMAE}(\%) &= \frac{\sum_{i=1}^S |y_{true,i} - y_{pred,i}|}{\sum_{i=1}^S |y_{true,i}|} \times 100(\%) \end{aligned} \quad (11)$$

The RRMSE results for all nine target curves are tabulated in Table 4. These results demonstrate that the stress-strain curves derived from the NN-generated designs generally exhibit strong alignment with the target curves. Analysis of the RRMSE for the best-matching designs reveals an average difference of 7.41% and a median difference of 5.20% between the target and generated design curves over all nine target curves. Notably, designs associated with Curve 3 display RRMSE values ranging from 3.77% to 4.06%, indicating a particularly high level of accuracy for this mechanical behavior. However, some curves, such as Curve 9, show higher variability in their generations, with RRMSE values reaching up to 14.2% for the third-best match. These findings suggest that while the generative model performs well in most cases, there is some variation in its accuracy across different mechanical situations. This variability may provide insights into the model’s strengths and limitations in replicating specific mechanical properties.

Table 4: RRMSE between the target curve and curves from generated designs. The first three best matches in RRMSE metric are shown.

	Curve 1	Curve 2	Curve 3	Curve 4	Curve 5	Curve 6	Curve 7	Curve 8	Curve 9
Best	5.20%	4.60%	3.77%	11.8%	4.92%	9.36%	8.86%	5.16%	13.1%
2nd	6.58%	4.77%	4.00%	20.0%	6.60%	10.4%	10.9%	9.53%	13.5%
3rd	7.25%	5.99%	4.06%	21.0%	7.10%	11.6%	11.6%	12.1%	14.2%

Fig. 12 provides a visual comparison between the target curves and the curves generated by our framework. For the majority of cases, the stress-strain curves produced by the generated designs closely align with the target curves, demonstrating the general effectiveness of our framework in capturing diverse mechanical behaviors. However, Curves 7 and 9 exhibit more noticeable deviations, indicating that certain mechanical behaviors pose greater challenges for our model to reproduce accurately. Of particular interest are the sudden jumps observed in Curves 3 and 8. While the generated curves approximate this behavior, they struggle to capture the precise moment and magnitude of these abrupt changes. The visual results corroborate the RRMSE values presented in Table 4, providing a comprehensive view of the model’s performance across various target mechanical behaviors. The analysis underscores both the strengths of our framework in reproducing a wide range of mechanical properties and the specific challenges that remain, particularly capturing the precise moment of the abrupt change in the mechanical behavior.

Following the RRMSE analysis, we employed the RMAE metric, as defined in Eq. (11), to further evaluate the similarity between the target curves and those derived from the generated designs. The RMAE values for the best match, second-best match, and third-best match were calculated and tabulated for comprehensive analysis. The results are summarized in Table 5. This metric complements the RRMSE analysis by offering a measure that is less sensitive to outliers, thereby providing a more robust assessment of the overall curve similarity. Additionally, RMAE offers a

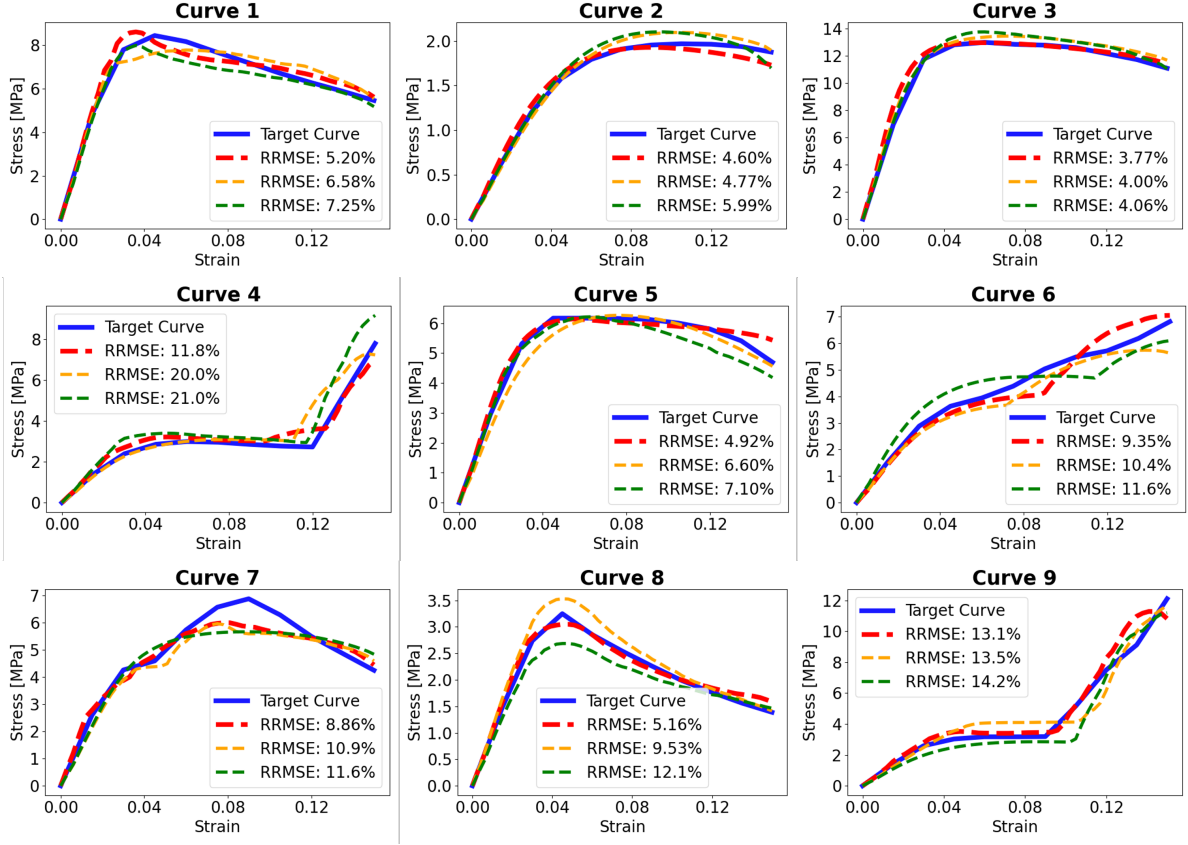


Figure 12: Comparison of target curves (solid blue) with curves from the three best-matching generated designs for each target curve, as measured by RRMSE. The dotted lines represent the generated designs, with red denoting the best match, orange the second-best match, and green the third-best match across all cases.

more intuitive interpretation of the average relative error between the target and generated curves. This dual-metric approach allows to capture different aspects of curve similarity, enhancing the reliability of our performance assessment.

Table 5: RMAE between the target curve and curves from generated designs. The first three best matches in RMAE metric are shown.

	Curve 1	Curve 2	Curve 3	Curve 4	Curve 5	Curve 6	Curve 7	Curve 8	Curve 9
Best	4.60%	4.03%	2.17%	10.7%	3.44%	8.07%	7.20%	4.41%	11.0%
2nd	5.63%	4.33%	3.57%	13.7%	5.00%	8.95%	9.36%	8.23%	13.5%
3rd	5.80%	5.04%	3.82%	19.1%	5.73%	10.2%	9.91%	10.2%	14.4%

The RMAE results presented in Table 5 exhibit a trend similar to the RRMSE analysis. For the best-matching designs across all nine target curves, the RMAE analysis reveals an average difference of 6.18% and a median difference of 4.60% between the target and generated-design curves.

Although RMAE generally yielded slightly lower values than RRMSE due to its reduced sensitivity to large individual errors, the relative performance across different target curves remained consistent between the two metrics. For instance, curves 2, 3, and 5 demonstrated low RMAE

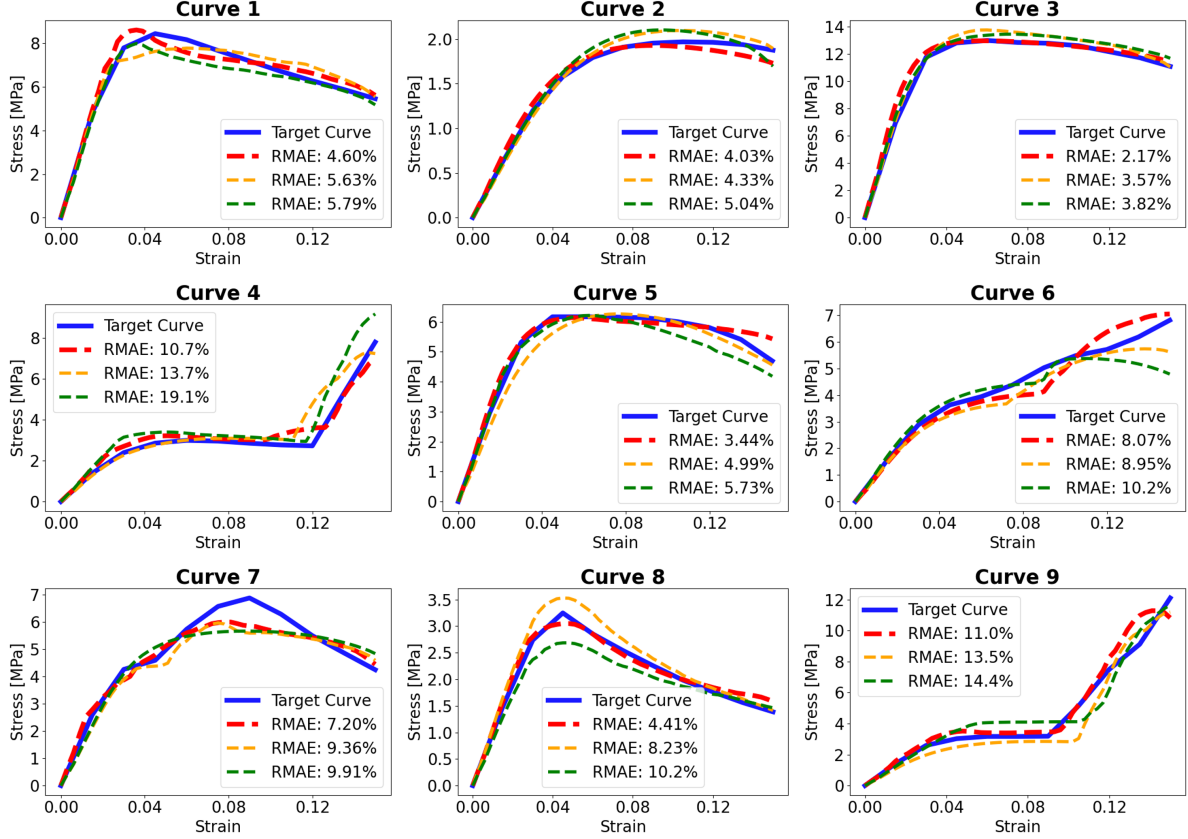


Figure 13: Comparison of target curves (solid blue) with curves from the three best-matching generated designs for each target curve, as measured by RMAE. The dotted lines represent the generated designs, with red denoting the best match, orange the second-best match, and green the third-best match across all cases.

values, corresponding to their low RRMSE values. This consistency underscores the alignment between the two metrics and suggests that the model is particularly adept at reproducing these specific mechanical behaviors. Conversely, curves with sudden changes, such as 4 and 9, exhibited relatively higher RMAE values, aligning with their RRMSE results. Despite these challenges, all cases maintained RMAE values below 11% for the best match, indicating reliable reproduction across various mechanical behaviors. Fig. 13 displays plots similar to those in Fig. 12, but using RMAE as the metric. Notably, the best-match designs identified by RRMSE and RMAE were identical for all nine target curves, further validating the consistency of our model’s performance across different error metrics. Consequently, the best-match designs for RMAE are also represented in Fig. 14.

Our framework demonstrates a remarkable capability to generate diverse and non-intuitive multi-material lattice designs, as illustrated in Fig. 14. Of particular interest is the best design for Curve 2, which presents a unique hourglass-like structure with intersecting curved elements. This design deviates from conventional lattice patterns, featuring a central diamond shape bordered by asymmetric curved members. Such non-intuitive structures highlight the AI model’s ability to explore complex design spaces beyond human preconceptions, potentially uncovering novel structures with desired mechanical properties. This competence in generating unexpected yet potentially high-performing designs accentuates the value of AI-driven approaches. These findings demonstrate the NN’s effectiveness in generating innovative designs that closely match target stress-strain

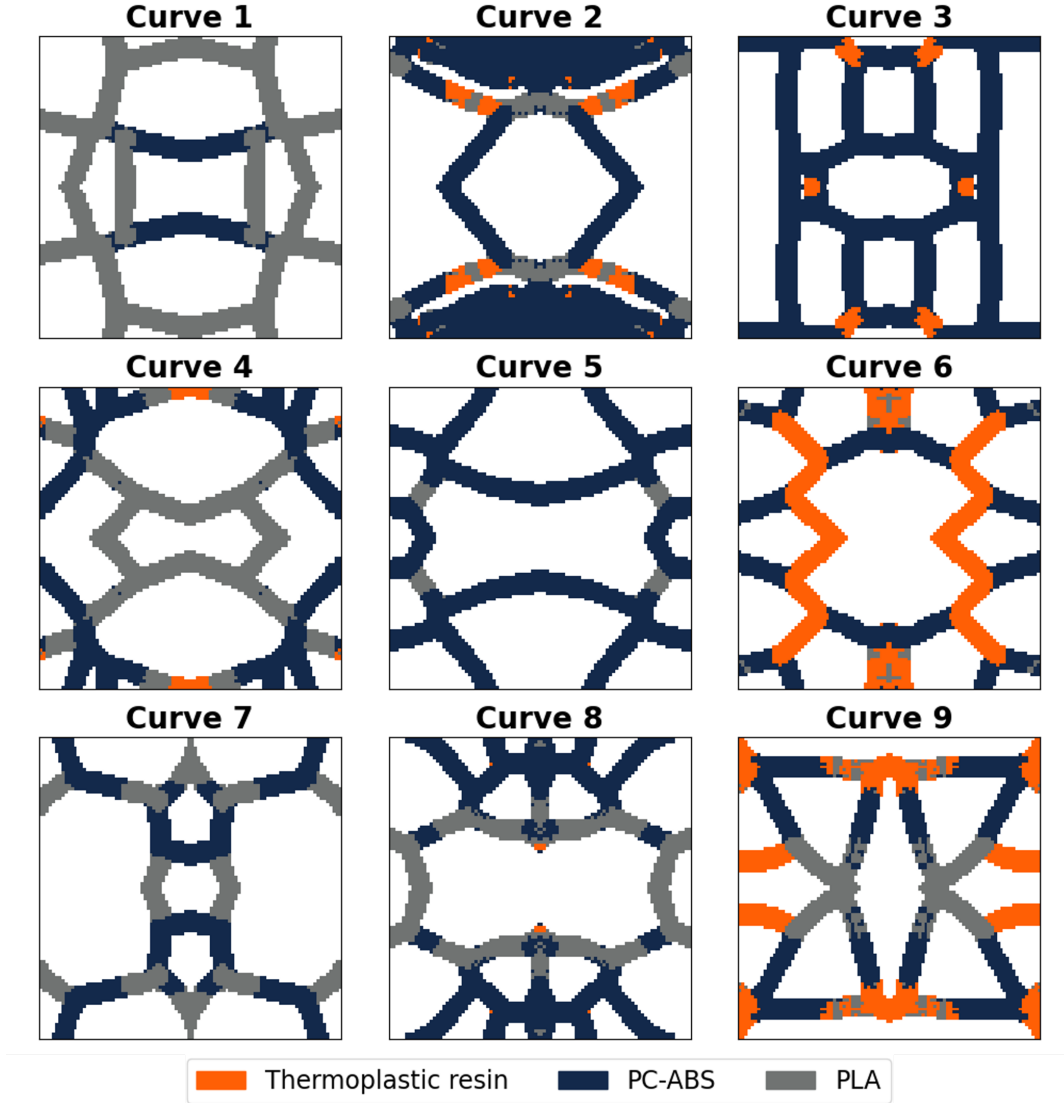


Figure 14: Designs that produced closest stress strain curve to the target curve measured by RRMSE and RMAE

curves, highlighting its potential for applications in topology optimization and additive manufacturing. The consistency of the generated designs, with an average of 7.41% RRMSE and 6.18% RMAE, underscores the robustness of this approach. However, cases like Curve 7, which show higher RRMSE, indicate areas for further improvement to enhance performance across a wider range of target curves.

The FEA validation confirms the capability of the NN-generated multi-material designs to achieve the desired non linear mechanical behavior, representing a significant advancement in efficient design generation for additive manufacturing. This method has the potential to reduce design iteration times and minimize material waste, offering a powerful tool for accelerating innovation in the field. Moreover, our neural network-based approach extends beyond the capabilities of traditional topology optimization methods [55], which are typically gradient-based and well-suited for linear responses. By leveraging deep learning techniques, our method effectively addresses non-linear phenomena such as large deformations and plasticity while able to generate multiple designs

per condition, opening up new possibilities in metamaterial design.

Finally, it is worth noting that the validation framework outlined in this section resembles the actual design framework that can be deployed in practice. After providing a designer engineer with adequately trained diffusion and structural identifier models, their inference will almost instantly provide many multi-material design candidates for the desired nonlinear behavior. Based on their additive manufacturability, a few will be chosen for quick forward finite element analysis to find the one most closely matching the original nonlinear behavior, which will be 3D printed and further experimentally tested. Since the training of the generative AI model on GPUs is usually done once, the trained learnable parameters (weights and biases) can be transferred to any low-end computing platform such as a laptop, and the multi-material design candidates can be inferred almost instantly for a given nonlinear response.

4. Conclusions and future work

The study presents a promising generative AI framework for multi-material lattice structure designs with tailored target responses. It demonstrates significant potential in fields requiring inverse-design problems, such as impact-resistant structures, additive manufacturing, topology optimization, and biomedical designs. The results show that the model can effectively produce multi-material designs that align with desired nonlinear stress-strain curves, bridging the gap between target performance and manufacturable outputs. While the framework shows considerable promise, areas remain for improvement to ensure consistent accuracy across all mechanical behaviors. We propose the following approaches to enhance the model’s reliability and generalizability. First, we suggest to expand the dataset size. It could be advantageous to incorporate a wider range of data that covers more mechanical behaviors and material choices to enhance the generalizability of NNs. Second, one could implement enhanced algorithms for the loss functions in both the diffusion model and the structure identifier, capturing the data to get refined predictions in the inference phase. Third, further improving the fidelity of the input finite element simulations by considering feature-size-dependent material properties induced by the additive manufacturing process employed to manufacture the multi-material structures [56, 57]. Lastly, integrate uncertainty quantification methods. Allowing the framework to predict the uncertainty of its creation by providing confidence intervals for the mechanical properties will enhance decision-making by allowing designers to assess the reliability of the generated designs, identify potential risks, and make informed choices regarding material use and design modifications.

In conclusion, this work, for the first time, demonstrates the effectiveness of a generative AI-based approach for creating multi-material designs with desired complex nonlinear mechanical behavior originating from large deformation and plasticity, and offering a significant advancement in computational design for additive and other advanced manufacturing processes. Our framework shows promise in revolutionizing inverse-design problems across various fields. Future efforts will address current limitations and extend the framework to more complex design scenarios, further pushing the boundaries of innovation in mechanics and materials science and engineering.

Replication of results

The data and source code supporting this study will be available in a public GitHub repository.

Conflict of interest

The authors declare that they have no conflict of interest.

Acknowledgements

The authors would like to thank the National Center for Supercomputing Applications (NCSA) at the University of Illinois, and particularly its Research Computing Directorate, the Industry Program, and the Center for Artificial Intelligence Innovation (CAII) for their support and hardware and software resources. This research is a part of the Delta research computing project, which is supported by the National Science Foundation (award OCI 2005572) and the State of Illinois, as well as the Illinois Computes program supported by the University of Illinois Urbana-Champaign and the University of Illinois System. We also extend our gratitude to Jan-Hendrik Bastek and Dennis M. Kochmann for their original work on the video diffusion model, and for their valuable insights provided through email correspondence.

CRedit author contributions

Jaewan Park: Conceptualization, Methodology, Software, Formal analysis, Investigation, Writing - Original Draft. **Shashank Kushwaha:** Conceptualization, Methodology, Software, Formal analysis, Investigation, Writing - Original Draft. **Junyan He:** Investigation, Supervision, Writing - Review & Editing. **Seid Koric:** Conceptualization, Methodology, Supervision, Resources, Writing - Original Draft, Funding Acquisition. **Qibang Liu:** Investigation, Writing - Review & Editing. **Iwona Jasiuk:** Supervision, Writing - Review & Editing. **Diab Abueidda:** Conceptualization, Methodology, Supervision, Writing - Review & Editing.

References

- [1] Aamer Nazir, Ozkan Gokcekaya, Kazi Md Masum Billah, Onur Ertugrul, Jingchao Jiang, Jiayu Sun, and Sajjad Hussain. Multi-material additive manufacturing: A systematic review of design, properties, applications, challenges, and 3d printing of materials and cellular metamaterials. *Materials & Design*, 226:111661, 2023.
- [2] Shakib Hyder Siddique, Paul J Hazell, Hongxu Wang, Juan P Escobedo, and Ali AH Ameri. Lessons from nature: 3d printed bio-inspired porous structures for impact energy absorption—a review. *Additive Manufacturing*, 58:103051, 2022.
- [3] Qi Pan, ShiTong Chen, FeiFei Chen, and XiangYang Zhu. Programmable soft bending actuators with auxetic metamaterials. *Science China Technological Sciences*, 63(12):2518–2526, 2020.
- [4] Elvan Dogan, Anant Bhusal, Berivan Cecen, and Amir K Miri. 3d printing metamaterials towards tissue engineering. *Applied materials today*, 20:100752, 2020.
- [5] Xiaoyang Zheng, Zhibing Fu, Kai Du, Chaoyang Wang, and Yong Yi. Minimal surface designs for porous materials: from microstructures to mechanical properties. *Journal of materials science*, 53:10194–10208, 2018.
- [6] Yifan Wang, Liuchi Li, Douglas Hofmann, José E Andrade, and Chiara Daraio. Structured fabrics with tunable mechanical properties. *Nature*, 596(7871):238–243, 2021.
- [7] F Scarpa, P Panayiotou, and G Tomlinson. Numerical and experimental uniaxial loading on in-plane auxetic honeycombs. *The Journal of Strain Analysis for Engineering Design*, 35(5):383–388, 2000.
- [8] A. Viswanath, M. Khalil, F. Al Maskari, W.J. Cantwell, and K.A. Khan. Harnessing buckling response to design lattice structures with improved buckling strength. *Materials & Design*, 232:112113, 2023.
- [9] Liang Xia and Piotr Breitkopf. Concurrent topology optimization design of material and structure within fe2 nonlinear multiscale analysis framework. *Computer Methods in Applied Mechanics and Engineering*, 278:524–542, 2014.
- [10] Akihiro Takezawa and Makoto Kobashi. Design methodology for porous composites with tunable thermal expansion produced by multi-material topology optimization and additive manufacturing. *Composites Part B: Engineering*, 131:21–29, 2017.
- [11] Diab W. Abueidda, Ziliang Kang, Seid Koric, Kai A. James, and Iwona M. Jasiuk. Topology optimization for three-dimensional elastoplastic architected materials using a path-dependent adjoint method. *International Journal for Numerical Methods in Engineering*, 122(8):1889–1910, 2021.
- [12] Qingliang Zeng, Shengyu Duan, Zeang Zhao, Pandeng Wang, and Hongshuai Lei. Inverse design of energy-absorbing metamaterials by topology optimization. *Advanced Science*, 10(4):2204977, 2023.

- [13] Miguel A Bessa, Piotr Glowacki, and Michael Houlder. Bayesian machine learning in metamaterial design: Fragile becomes supercompressible. *Advanced Materials*, 31(48):1904845, 2019.
- [14] Siddhant Kumar, Stephanie Tan, Li Zheng, and Dennis M Kochmann. Inverse-designed spinodoid metamaterials. *npj Computational Materials*, 6(1):73, 2020.
- [15] Jackson K Wilt, Charles Yang, and Grace X Gu. Accelerating auxetic metamaterial design with deep learning. *Advanced Engineering Materials*, 22(5):1901266, 2020.
- [16] Hunter T Kollmann, Diab W Abueidda, Seid Koric, Erman Guleryuz, and Nahil A Sobh. Deep learning for topology optimization of 2d metamaterials. *Materials & Design*, 196:109098, 2020.
- [17] Diab W Abueidda, Seid Koric, and Nahil A Sobh. Topology optimization of 2d structures with nonlinearities using deep learning. *Computers & Structures*, 237:106283, 2020.
- [18] Shashank Kushwaha, Jaewan Park, Seid Koric, Junyan He, Iwona Jasiuk, and Diab Abueidda. Advanced deep operator networks to predict multiphysics solution fields in materials processing and additive manufacturing. *Additive Manufacturing*, page 104266, 2024.
- [19] Xiaoyang Zheng, Xubo Zhang, Ta-Te Chen, and Ikumu Watanabe. Deep learning in mechanical metamaterials: From prediction and generation to inverse design. *Advanced Materials*, 35(45):2302530, 2023.
- [20] Kai A James and Haim Waisman. Topology optimization of viscoelastic structures using a time-dependent adjoint method. *Computer Methods in Applied Mechanics and Engineering*, 285:166–187, 2015.
- [21] Corey M Parrott, Diab W Abueidda, and Kai A James. Multidisciplinary topology optimization using generative adversarial networks for physics-based design enhancement. *Journal of Mechanical Design*, 145(6):061704, 2023.
- [22] Corey M Parrott, Diab W Abueidda, and Kai A James. Multi-head self-attention generative adversarial networks for multiphysics topology optimization. *AIAA Journal*, 61(2):726–738, 2023.
- [23] Yunwei Mao, Qi He, and Xuanhe Zhao. Designing complex architected materials with generative adversarial networks. *Science advances*, 6(17):eaaz4169, 2020.
- [24] Xiaoyang Zheng, Ta-Te Chen, Xiaofeng Guo, Sadaki Samitsu, and Ikumu Watanabe. Controllable inverse design of auxetic metamaterials using deep learning. *Materials & Design*, 211:110178, 2021.
- [25] Wei Ma, Feng Cheng, Yihao Xu, Qinlong Wen, and Yongmin Liu. Probabilistic representation and inverse design of metamaterials based on a deep generative model with semi-supervised learning strategy. *Advanced Materials*, 31(35):1901111, 2019.
- [26] Liwei Wang, Yu-Chin Chan, Faez Ahmed, Zhao Liu, Ping Zhu, and Wei Chen. Deep generative modeling for mechanistic-based learning and design of metamaterial systems. *Computer Methods in Applied Mechanics and Engineering*, 372:113377, 2020.
- [27] Chan Soo Ha, Desheng Yao, Zhenpeng Xu, Chenang Liu, Han Liu, Daniel Elkins, Matthew Kile, Vikram Deshpande, Zhenyu Kong, Mathieu Bauchy, et al. Rapid inverse design of metamaterials based on prescribed mechanical behavior through machine learning. *Nature Communications*, 14(1):5765, 2023.
- [28] Jonathan Ho, Ajay Jain, and Pieter Abbeel. Denoising diffusion probabilistic models. *Advances in neural information processing systems*, 33:6840–6851, 2020. doi: doi.org/10.48550/arXiv.2006.11239.
- [29] Prafulla Dhariwal and Alexander Nichol. Diffusion models beat gans on image synthesis. *Advances in neural information processing systems*, 34:8780–8794, 2021. doi: doi.org/10.48550/arXiv.2105.05233.
- [30] Jonathan Ho and Tim Salimans. Classifier-free diffusion guidance. *arXiv preprint arXiv:2207.12598*, 2022.
- [31] Aditya Ramesh, Prafulla Dhariwal, Alex Nichol, Casey Chu, and Mark Chen. Hierarchical text-conditional image generation with clip latents. *arXiv preprint arXiv:2204.06125*, 1(2):3, 2022.
- [32] James Betker, Gabriel Goh, Li Jing, Tim Brooks, Jianfeng Wang, Linjie Li, Long Ouyang, Juntang Zhuang, Joyce Lee, Yufei Guo, et al. Improving image generation with better captions. *Computer Science*. <https://cdn.openai.com/papers/dall-e-3.pdf>, 2(3):8, 2023.
- [33] Tim Brooks, Bill Peebles, Connor Holmes, Will DePue, Yufei Guo, Li Jing, David Schnurr, Joe Taylor, Troy Luhman, Eric Luhman, Clarence Ng, Ricky Wang, and Aditya Ramesh. Video generation models as world simulators. 2024. URL <https://openai.com/research/video-generation-models-as-world-simulators>.
- [34] Yixin Liu, Kai Zhang, Yuan Li, Zhiling Yan, Chujie Gao, Ruoxi Chen, Zhengqing Yuan, Yue Huang, Hanchi Sun, Jianfeng Gao, et al. Sora: A review on background, technology, limitations, and opportunities of large vision models. *arXiv preprint arXiv:2402.17177*, 2024.
- [35] Chitwan Saharia, William Chan, Saurabh Saxena, Lala Li, Jay Whang, Emily L Denton, Kamyar Ghasemipour, Raphael Gontijo Lopes, Burcu Karagol Ayan, Tim Salimans, Jonathan Ho, David J Fleet, and Mohammad Norouzi. Photorealistic text-to-image diffusion models with deep language understanding. In S. Koyejo, S. Mohamed, A. Agarwal, D. Belgrave, K. Cho, and A. Oh, editors, *Advances in Neural Information Processing Systems*, volume 35, pages 36479–36494. Curran Associates, Inc., 2022. URL https://proceedings.neurips.cc/paper_files/paper/2022/file/ec795aeadae0b7d230fa35cbaf04c041-Paper-Conference.pdf.
- [36] Jonathan Ho, William Chan, Chitwan Saharia, Jay Whang, Ruiqi Gao, Alexey Gritsenko, Diederik P Kingma, Ben Poole, Mohammad Norouzi, David J Fleet, et al. Imagen video: High definition video generation with diffusion models. *arXiv preprint arXiv:2210.02303*, 2022.
- [37] Robin Rombach, Andreas Blattmann, Dominik Lorenz, Patrick Esser, and Björn Ommer. High-resolution image synthesis with latent diffusion models, 2022.
- [38] Dustin Podell, Zion English, Kyle Lacey, Andreas Blattmann, Tim Dockhorn, Jonas Müller, Joe Penna, and Robin Rombach. Sdxl: Improving latent diffusion models for high-resolution image synthesis. *arXiv preprint arXiv:2307.01952*, 2023.
- [39] Axel Sauer, Frederic Boesel, Tim Dockhorn, Andreas Blattmann, Patrick Esser, and Robin Rombach. Fast high-resolution image synthesis with latent adversarial diffusion distillation. *arXiv preprint arXiv:2403.12015*, 2024.
- [40] Tomer Weiss, Eduardo Mayo Yanes, Sabyasachi Chakraborty, Luca Cosmo, Alex M Bronstein, and Renana Gershoni-Poranne. Guided diffusion for inverse molecular design. *Nature Computational Science*, 3(10):873–882, 2023.
- [41] Gang Liu, Jiaxin Xu, Tengfei Luo, and Meng Jiang. Inverse molecular design with multi-conditional diffusion guidance. *arXiv preprint arXiv:2401.13858*, 2024.
- [42] Fan Bao, Min Zhao, Zhongkai Hao, Peiyao Li, Chongxuan Li, and Jun Zhu. Equivariant energy-guided sde for inverse molecular design. In *The eleventh international conference on learning representations*, 2022.
- [43] Jan-Hendrik Bastek and Dennis M Kochmann. Inverse design of nonlinear mechanical metamaterials via video denoising diffusion models. *Nature Machine Intelligence*, 5(12):1466–1475, 2023.
- [44] Yanyan Yang, Lili Wang, Xiaoya Zhai, Kai Chen, Wenming Wu, Yunkai Zhao, Ligang Liu, and Xiao-Ming Fu. Guided diffusion for fast inverse design of density-based mechanical metamaterials. *arXiv preprint arXiv:2401.13570*, 2024.

- [45] Yayati Jadhav, Joeseeph Berthel, Chunshan Hu, Rahul Panat, Jack Beuth, and Amir Barati Farimani. Generative lattice units with 3d diffusion for inverse design: Glu3d. *Advanced Functional Materials*, page 2404165, 2024.
- [46] Nikolaos N Vlassis and WaiChing Sun. Denoising diffusion algorithm for inverse design of microstructures with fine-tuned nonlinear material properties. *Computer Methods in Applied Mechanics and Engineering*, 413:116126, 2023.
- [47] Daniel Wines, Tian Xie, and Kamal Choudhary. Inverse design of next-generation superconductors using data-driven deep generative models. *The Journal of Physical Chemistry Letters*, 14(29):6630–6638, 2023.
- [48] Chengquan Zhong, Jingzi Zhang, Yuelin Wang, Yanwu Long, Pengzhou Zhu, Jiakai Liu, Kailong Hu, Junjie Chen, and Xi Lin. High-performance diffusion model for inverse design of high T_c superconductors with effective doping and accurate stoichiometry. *InfoMat*, 6(5): e12519, 2024.
- [49] Georges Voronoï. Nouvelles applications des parametres continus a la theorie des forms quadratiques. deuxieme memoire: Recherchees sur les paralleloedres primitifs. *J. reine angew. Math.*, 134:198–287, 1908.
- [50] SIMULIA Dassault Systèmes. Abaqus/standard user's manual version 2024, 2024.
- [51] Shashank Kushwaha, Junyan He, Diab Abueidda, and Iwona Jasiuk. Designing impact-resistant bio-inspired low-porosity structures using neural networks. *Journal of Materials Research and Technology*, 27:767–779, 2023.
- [52] Lishuai Jin, Romik Khajehtourian, Jochen Mueller, Ahmad Rafsanjani, Vincent Tournat, Katia Bertoldi, and Dennis M Kochmann. Guided transition waves in multistable mechanical metamaterials. *Proceedings of the National Academy of Sciences*, 117(5):2319–2325, 2020.
- [53] Ross Johnston and Zafer Kazancı. Analysis of additively manufactured (3d printed) dual-material auxetic structures under compression. *Additive Manufacturing*, 38:101783, 2021.
- [54] Yann Soon, Soo Ngee Koh, and Chai Kiat Yeo. Noisy speech enhancement using discrete cosine transform. *Speech communication*, 24(3): 249–257, 1998.
- [55] Zhengtong Han and Kai Wei. Multi-material topology optimization and additive manufacturing for metamaterials incorporating double negative indexes of poisson's ratio and thermal expansion. *Additive Manufacturing*, 54:102742, 2022.
- [56] Junyan He, Shashank Kushwaha, Mahmoud A Mahrous, Diab Abueidda, Eric Faierson, and Iwona Jasiuk. Size-dependence of am ti–6al–4v: Experimental characterization and applications in thin-walled structures simulations. *Thin-Walled Structures*, 187:110722, 2023.
- [57] Charul Chadha, Gabriel Olaivar, Mahmoud A Mahrous, Albert E Patterson, and Iwona Jasiuk. Exploring the effect of specimen size on elastic properties of fused-filament-fabrication-printed polycarbonate and thermoplastic polyurethane. *Materials*, 17(11):2677, 2024.

Appendix

Material properties

The materials used in this work are as follows: thermoplastic acetal homopolymer resin, PC-ABS, and PLA. In the elastic regime, the thermoplastic acetal homopolymer resin has a Young's modulus of 2306 MPa and a Poisson's ratio of 0.35. For PC-ABS, the Young's modulus was set to 2500 MPa and a Poisson's ratio of 0.35. Lastly, for PLA, the Young's modulus was set to 2300 MPa and the Poisson's ratio was set to 0.35. The plastic regime for each material was plotted as shown in Fig. 15.

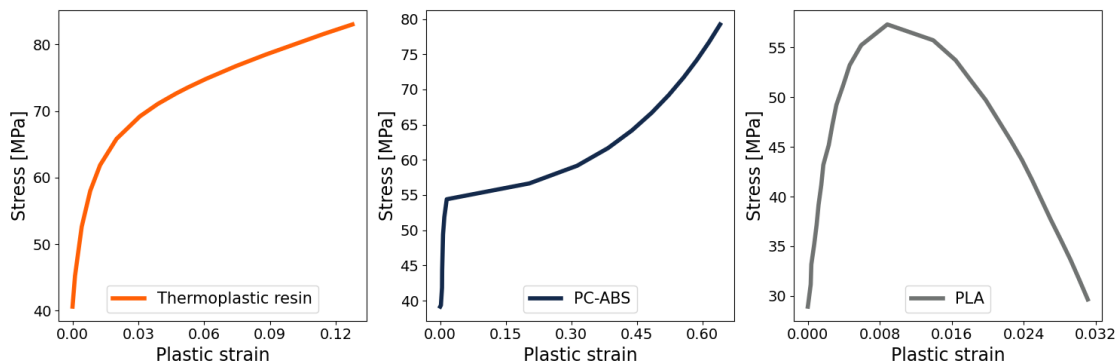


Figure 15: Stress and plastic stain plots for each material used in the work.